A&A 510, A7 (2010)
DOI: 10.1051/0004-6361/200912888

Astronomy & Astrophysics

Measuring cosmic shear with the ring statistics

T. Eifler[1], P. Schneider[1], and E. Krause[2,1]

[1] Argelander-Institut für Astronomie, Universität Bonn, Auf dem Hügel 71, 53121 Bonn, Germany
e-mail: tim.eifler@astro.uni-bonn.de
[2] California Institute of Technology, M/C 350-17, Pasadena, California 91125, USA

Received 14 July 2009 / Accepted 10 November 2009

ABSTRACT

Context. Commonly used methods of decomposing E- and B-modes in cosmic shear, namely the aperture mass dispersion and the E/B-mode shear correlation function, suffer from incomplete knowledge of the two-point correlation function (2PCF) on very small and/or very large scales. The ring statistics, the most recently developed cosmic shear measure, improves on this issue and is able to decompose E- and B-modes using a 2PCF measured on a finite interval.
Aims. First, we improve on the ring statistics' filter function over the signal-to-noise ratio (S/N). Second, we examine the ability of the ring statistics to constrain cosmology and compare the results to cosmological constraints obtained with the aperture mass dispersion. Third, we use the ring statistics to measure a cosmic shear signal from CFHTLS (Canada-France-Hawaii Telescope Legacy Survey) data.
Methods. We consider a scale-dependent filter function for the ring statistics, which improves its S/N. To examine the information content of the ring statistics, we employed ray-tracing simulations and developed an expression of the ring statistics' covariance in terms of a 2PCF covariance. We performed a likelihood analysis with simulated data for the ring statistics in the Ω_m-σ_8 parameter space and compared the information content of ring statistics and aperture mass dispersion. Regarding our third aim, we used the 2PCF of the latest CFHTLS analysis to calculate the ring statistics and its error bars.
Results. Although the scale-dependent filter function improves the S/N of the ring statistics, the S/N of the aperture mass dispersion is higher. In addition, we show that filter functions exist that decompose E- and B-modes using a finite range of 2PCFs (EB-statistics) and have higher S/N than the ring statistics. However, we find that data points of the latter are significantly less correlated than data points of the aperture mass dispersion and the EB-statistics. As a consequence the ring statistics is an ideal tool for identifying remaining systematics accurately as a function of angular scale. We use the ring statistics to measure a E- and B-mode shear signal from CFHTLS data.

Key words. gravitational lensing: weak – large-scale structure of Universe – methods: data analysis

1. Introduction

Cosmic shear was first detected in 2000 (Bacon et al. 2000; Kaiser et al. 2000; van Waerbeke et al. 2000; Wittman et al. 2000) and has progressed to becoming a valuable source of cosmological information. The latest results (e.g., van Waerbeke et al. 2005; Semboloni et al. 2006; Hoekstra et al. 2006; Schrabback et al. 2007; Hetterscheidt et al. 2007; Massey et al. 2007b; Fu et al. 2008) already indicate its high potential of constraining cosmological parameters, which will be enhanced by large upcoming surveys like Pan-STARRS, KIDS, DES or Euclid.

An important step in any cosmic shear analysis is the decomposition into E- and B-modes, where, to leading order, gravitational lensing only creates E-modes. In principle, B-modes can arise from the limited validity of the Born approximation (Jain et al. 2000; Hilbert et al. 2009) or redshift source clustering (Schneider et al. 2002b). Another possible source can be astrophysical contaminations, such as intrinsic alignment of source galaxies. King & Schneider (2003) show how to separate the cosmic shear signal from intrinsic alignment contaminations if redshift information is available. The strength of B-modes coming from these effects are examined through numerical simulations. Although the results differ (e.g. Heavens et al. 2000; Crittenden et al. 2001; Jing 2002), the observed B-mode amplitude is higher than expected from the foregoing explanations. Shape-shear correlation (Hirata & Seljak 2004) is another astrophysical contamination that can cause B-modes. Joachimi & Schneider (2008, 2009) show how to exclude the contaminated scales, again using redshift information.

Most likely, B-modes indicate remaining systematics in the observations and data analysis; in particular, they can result from an insufficient PSF-correction. The Shear TEsting Program (STEP) has significantly improved on this issue (for latest results see Heymans et al. 2006; Massey et al. 2007a), but the accuracy of the ellipticity measurements must be improved further to meet the requirements of precision cosmology.

The identification of remaining systematics (B-modes) will be important especially for future surveys, where the statistical errors will be significantly smaller. Therefore, decomposing the shear field into E- and B-modes must not be affected from inherent deficits. The most commonly used methods for an E- and B-mode decomposition, the aperture mass dispersion and the E/B-mode shear correlation function, require the shear two-point correlation (2PCF from now on) to be known down to arbitrarily small or up to arbitrary large angular separations, respectively. This is not possible in practice, and as a consequence the corresponding methods do not separate E- and B-modes properly on

all angular scales. A detailed analysis of this issue can be found in Kilbinger et al. (2006) (hereafter KSE06).

Most cosmic shear analyses, e.g. Massey et al. (2007b) and Fu et al. (2008) (hereafter FSH08), simulate 2PCFs from a theoretical model of P_κ to account for the scales on which the 2PCF cannot be obtained from the data. This ansatz is problematic, since one explicitly assumes that the corresponding scales are free of B-modes. In addition, the assumed cosmology in the theoretical power spectrum can bias the results.

The ring statistics (Schneider & Kilbinger 2007, hereafter SK07) provides a new method to perform an E-/B-mode decomposition using a 2PCF measured over a finite angular range $[\vartheta_{\rm min};\vartheta_{\rm max}]$. In this paper we examine the ring statistics in detail. More precisely we improve the ring statistics' filter function with respect to its S/N and examine its ability to constrain cosmological parameters. Furthermore, we construct a filter functions which has higher S/N than the ring statistics but still decomposes E/B-modes with a 2PCF measured over a finite range. We will refer to this as EB-statistics.

Due to the fact that the ring statistics' data points show significantly lower correlation than data points of the aperture mass dispersion and the EB-statistics, it provides an ideal tool to identify remaining systematics in cosmic shear surveys depending on the angular scale. We employ the ring statistics to identify B-modes in the CFHTLS survey.

The paper is structured as follows: In Sect. 2 we start with the basics of second-order cosmic shear measures, followed by the main concepts of the ring statistics in Sect. 3. We derive a formula to calculate the ring statistics' covariance from a 2PCF covariance in Sect. 5 and also compare the correlation coefficients of ring statistics, aperture mass dispersion, and EB-statistics in this section. In the same section we examine the S/N of the ring statistics and compare it to the other measures. More interesting than the S/N however, is the ability of a measure to constrain cosmology. This, in addition to the S/N, depends on the correlation of the individual data points. In order to quantify this accurately, we perform a likelihood analysis in Sect. 6 for the ring statistics, aperture mass dispersion and EB-statistics using data from ray-tracing simulations. The results of our analysis of CFHTLS data using the ring statistics are presented in Sect. 7 followed by our conclusions in Sect. 8.

2. Two-point statistics of cosmic shear

In this section we briefly review the basics of second-order cosmic shear measures. For more details on this topic the reader is referred to Bartelmann & Schneider (2001); Schneider et al. (2002a,b); van Waerbeke & Mellier (2003); Munshi et al. (2008).

To measure the shear signal we define $\boldsymbol{\vartheta}$ as the connecting vector of two galaxy centers and specify tangential and cross-component of the shear γ as

$$\gamma_{\rm t} = -{\rm Re}\left(\gamma {\rm e}^{-2{\rm i}\varphi}\right) \qquad \text{and} \qquad \gamma_\times = -{\rm Im}\left(\gamma {\rm e}^{-2{\rm i}\varphi}\right), \tag{1}$$

where φ is the polar angle of $\boldsymbol{\vartheta}$. The 2PCFs depend only on the absolute value of $\boldsymbol{\vartheta}$. They are defined in terms of the shear and can be related to the power spectra $P_{\rm E}$ and $P_{\rm B}$ (Schneider et al. 2002b)

$$\xi_\pm(\vartheta) \equiv \langle\gamma_{\rm t}\gamma_{\rm t}\rangle(\vartheta) \pm \langle\gamma_\times\gamma_\times\rangle(\vartheta) \tag{2}$$

$$= \int_0^\infty \frac{{\rm d}\ell\,\ell}{2\pi} J_{0/4}(\ell\vartheta)\ [P_{\rm E}(\ell) \pm P_{\rm B}(\ell)]\,, \tag{3}$$

with J_n denoting the nth order Bessel-function.

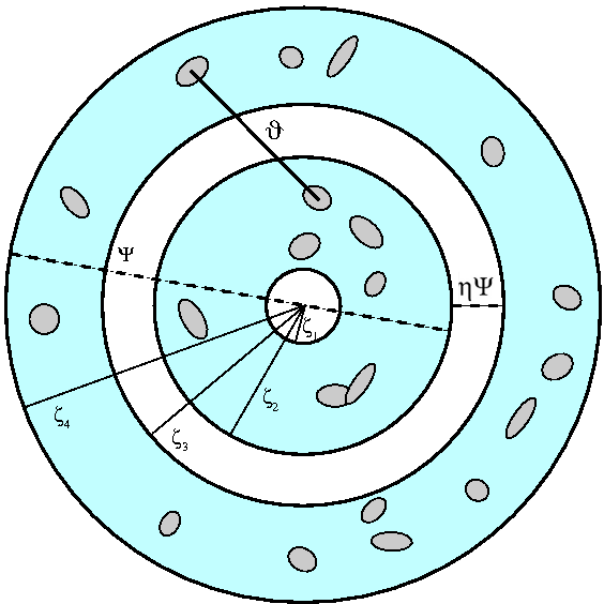

Fig. 1. This figure illustrates the basic idea of the ring statistics and how it can be obtained from the 2PCF of cosmic shear. We measure the 2PCF of each galaxy in the inner ring with all galaxies in the outer ring. For a given argument of the ring statistics Ψ, the angular separation of the required 2PCFs extends over $\eta\Psi \le \vartheta \le \Psi$. The meaning of η and its possible values are further explained in the text. The ring statistics is then calculated as an integral over the 2PCF with the filter functions $Z_\pm(\vartheta,\eta)$.

Starting from the 2PCF as the basic observable quantity, there exist several methods to decompose E-modes and B-modes, such as the E/B-mode shear correlation function or the aperture mass dispersion (e.g. Crittenden et al. 2002; Schneider et al. 2002b). The latter can be calculated as

$$\left\langle M^2_{\rm ap/\perp}\right\rangle(\theta) = \frac{1}{2}\int_0^{2\theta}\frac{{\rm d}\vartheta\,\vartheta}{\theta^2}\left[\xi_+(\vartheta)T_+\left(\frac{\vartheta}{\theta}\right) \pm \xi_-(\vartheta)T_-\left(\frac{\vartheta}{\theta}\right)\right]. \tag{4}$$

The filter functions read

$$T_+(x) = \left\{\frac{6(2-15x^2)}{5}\left[1-\frac{2}{\pi}\arcsin\left(\frac{x}{2}\right)\right] + \frac{x\sqrt{4-x^2}}{100\pi}(120 + 2320x^2 - 754x^4 + 132x^6 - 9x^8)\right\}{\rm H}(2-x), \tag{5}$$

$$T_-(x) = \frac{192}{35\pi}x^3\left(1-\frac{x^2}{4}\right)^{7/2}{\rm H}(2-x), \tag{6}$$

with H being the Heaviside step function. Decomposing E- and B-modes with the either the aperture mass dispersion or the E/B-mode shear correlation function requires that the 2PCF is either measured down to arbitrary small or large angular separation, respectively. For further details on this problem the reader is referred to KSE06.

3. The ring statistics

To circumvent the aforementioned difficulties SK07 introduced the ring statistics whose second-order moments $(\langle\mathcal{RR}_{\rm E}\rangle, \langle\mathcal{RR}_{\rm B}\rangle)$ decompose E- and B-modes properly using 2PCFs measured on a finite interval $[\vartheta_{\rm min};\vartheta_{\rm max}]$. The quantity $\langle\mathcal{RR}_{\rm E}\rangle$ can be interpreted as the correlator of the shear measured from galaxy pairs which are located inside two concentric rings (see Fig. 1). Their

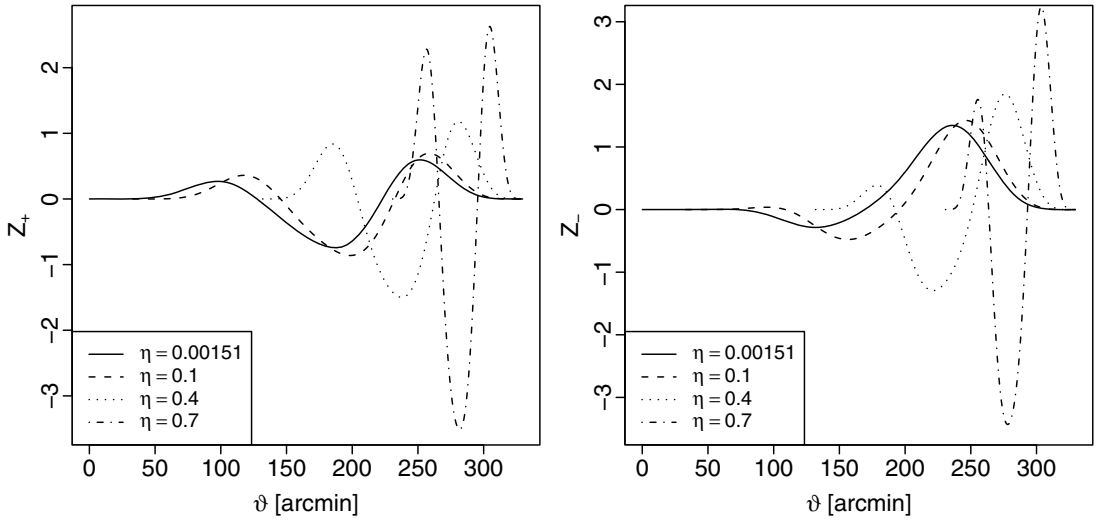

Fig. 2. This plot shows the filter functions Z_+ (*left*) and Z_- (*right*) depending on ϑ for four different choices of η: $\vartheta_{\rm min}/\Psi = 0.00151$ (*solid*), 0.1 (*dashed*), 0.4 (*dotted*), 0.7 (*dotted dashed*).

annuli are chosen as follows: $\zeta_1 \leq \theta_1 \leq \zeta_2$ for the first ring and $\zeta_3 \leq \theta_2 \leq \zeta_4$ for the second. The rings are non-overlapping, i.e. $\zeta_i < \zeta_j$ if $i < j$. The argument of the rings statistics is named $\Psi = \zeta_2 + \zeta_4$ and only 2PCFs with $\vartheta \leq \Psi$ enter in the calculation of $\langle \mathcal{RR}_{\rm E}\rangle$. In addition, the ring statistics depends on a parameter η quantifying the separation between outer and inner ring, i.e. $\eta/\Psi = \zeta_3 - \zeta_2$. In order to calculate the ring statistics properly from a set of 2PCFs within $[\vartheta_{\rm min}; \vartheta_{\rm max}]$ it is required that Ψ does not exceed $\vartheta_{\rm max}$ and that $\vartheta_{\rm min}/\Psi \leq \eta < 1$.

Following the derivation of SK07 the E- and B-mode decomposition of the ring statistics can be obtained from the 2PCF as

$$\langle \mathcal{RR}_{\rm E}\rangle(\Psi) = \int_{\eta\Psi}^{\Psi} \frac{{\rm d}\vartheta}{2\,\vartheta} \left[\xi_+(\vartheta)\, Z_+(\vartheta,\eta) + \xi_-(\vartheta)\, Z_-(\vartheta,\eta)\right], \quad (7)$$

$$\langle \mathcal{RR}_{\rm B}\rangle(\Psi) = \int_{\eta\Psi}^{\Psi} \frac{{\rm d}\vartheta}{2\,\vartheta} \left[\xi_+(\vartheta)\, Z_+(\vartheta,\eta) - \xi_-(\vartheta)\, Z_-(\vartheta,\eta)\right]. \quad (8)$$

The functions $Z_\pm$ are defined in SK07, and we plot them in Fig. 2 for four different η, i.e. $\vartheta_{\rm min}/\Psi = 0.00151, 0.1, 0.4, 0.7$.

Similar to the case of the aperture mass dispersion, $\langle \mathcal{RR}_{\rm E}\rangle$ can be related to the E-mode power spectrum. Inserting Eq. (3), into Eq. (7) gives

$$\langle \mathcal{RR}_{\rm E}\rangle(\Psi) = \int_0^\infty \frac{{\rm d}\ell\,\ell}{2\pi}\, P_{\rm E}(\ell)\, \mathcal{W}_{\rm E}(\ell\Psi,\eta) \quad (9)$$

with

$$\mathcal{W}_{\rm E}(\ell\Psi,\eta) = \int_{\eta\Psi}^{\Psi} \frac{{\rm d}\vartheta}{2\vartheta} \left[J_0(\ell\vartheta)\, Z_+(\vartheta,\eta) + J_4(\ell\vartheta)\, Z_-(\vartheta,\eta)\right]. \quad (10)$$

When calculating $\langle \mathcal{RR}_{\rm E}\rangle$ for different arguments Ψ, we distinguish two cases for η. It can be fixed to a specific value or it can vary according to Ψ, in particular $\eta = \vartheta_{\rm min}/\Psi$. We will refer to the latter case as a scale-dependent η. Here, the lower limit in the integrals of Eqs. (7) and (8) is equal to $\vartheta_{\rm min}$ which implies that all 2PCFs in the interval $[\vartheta_{\rm min}; \Psi]$ are included in the calculation. The choice of $\eta = \vartheta_{\rm min}/\Psi$ should give a higher S/N compared to a fixed η for the reason that more galaxy pairs are included which reduces the statistical noise. In SK07 the authors hold η fixed, which implies that η must be chosen as small as possible in order to obtain a high signal.

Choosing a fixed η has a second disadvantage. The lower limit in the integrals Eqs. (7) and (8) cannot be smaller than $\vartheta_{\rm min}$, i.e. $\eta\Psi \geq \vartheta_{\rm min}$. Vice versa, this implies that $\Psi \geq \vartheta_{\rm min}/\eta$. Fixing η to a low value (in order to increase the S/N) implies that Ψ is restricted to larger scales. This trade-off between S/N and small-scale sensitivity can be overcome when relaxing the condition of a fixed η.

4. General E/B-mode decomposition on a finite interval

The ring statistics described in the last section is the special case of a general E/B-mode decomposition. According to SK07 this general EB-statistics can be defined as

$$E = \frac{1}{2}\int_0^\infty {\rm d}\vartheta\,\vartheta \left[\xi_+(\vartheta) T_+(\vartheta) + \xi_-(\vartheta) T_-(\vartheta)\right], \quad (11)$$

$$B = \frac{1}{2}\int_0^\infty {\rm d}\vartheta\,\vartheta \left[\xi_+(\vartheta) T_+(\vartheta) - \xi_-(\vartheta) T_-(\vartheta)\right]. \quad (12)$$

To provide a clean separation of E- and B-modes using a 2PCF measured over a finite interval, the following conditions must be fulfilled (see SK07 for the exact derivation). Starting from an arbitrary function $T_+(\vartheta)$, which is zero outside the interval $[\vartheta_{\rm min}; \vartheta_{\rm max}]$, the constraints

$$\int_{\vartheta_{\rm min}}^{\vartheta_{\rm max}} {\rm d}\vartheta\,\vartheta T_+(\vartheta) = 0 = \int_{\vartheta_{\rm min}}^{\vartheta_{\rm max}} {\rm d}\vartheta\,\vartheta^3 T_-(\vartheta) \quad (13)$$

must hold. For a so constructed filter function $T_+(\vartheta)$ a corresponding filter function $T_-(\vartheta)$ can be calculated as

$$T_-(\vartheta) = T_+(\vartheta) + 4\int_{\vartheta_{\rm min}}^{\vartheta} {\rm d}\theta\,\frac{\theta}{\vartheta^2} T_+(\theta)\left[1 - 3\left(\frac{\theta}{\vartheta}\right)^2\right]. \quad (14)$$

Conversely, one can construct T_+ for a given T_-.

The expressions for T_+ and T_- used in this paper are given in the Appendix. We calculate the EB-statistics according to Eq. (11) and compare the results to the ring statistics. Note that this EB-statistics can be optimized, e.g., with respect to its S/N

or its ability to constrain cosmology. For more details on this topic the reader is referred to Fu & Kilbinger (2009).

In this paper, the EB-statistics is calculated as a function of Ψ. Similar to the ring statistics, Ψ denotes the maximum angular scale of 2PCFs which enter in the calculation of $E(\Psi)$.

5. Covariance and *S/N*

For our further analysis we have to derive a formula to calculate the covariance of ring statistics and EB-statistics. A corresponding expression for $\langle M_{\rm ap}^2\rangle$ reads (see e.g. Schneider et al. 2002b).

$$\mathrm{C}_{\mathcal{M}}(\theta_k,\theta_l)) = \frac{1}{4}\sum_{i=1}^{I}\sum_{j=1}^{J}\frac{\Delta\vartheta_i\Delta\vartheta_j}{\theta_k^2\theta_l^2}\,\vartheta_i\vartheta_j \times\left[\sum_{m,n=+,-}T_m\left(\frac{\vartheta_i}{\theta_k}\right)\,T_n\left(\frac{\vartheta_j}{\theta_l}\right)\mathrm{C}_{mn}(\vartheta_i,\vartheta_j)\right], \quad (15)$$

with $\mathrm{C}_{mn}(\vartheta_i,\vartheta_j)$ denoting the 2PCF covariance. Here, the upper limits I and J are chosen such that $\vartheta_i \le 2\theta_k$ and $\vartheta_j \le 2\theta_l$. The ring statistics' covariance is defined as

$$\mathrm{C}_{\mathcal{R}}(\Psi_k,\Psi_l) = \left\langle\hat{R}_{\rm E}^2(\Psi_k)\,\hat{R}_{\rm E}^2(\Psi_l)\right\rangle - \langle\mathcal{RR}_{\rm E}\rangle(\Psi_k)\,\langle\mathcal{RR}_{\rm E}\rangle(\Psi_l), \quad (16)$$

where $\hat{R}_{\rm E}^2$ denotes the estimator of the ring statistics. To calculate this estimator from a binned 2PCF data vector with bin width $\Delta\vartheta_i$ we replace the integrals in Eq. (7) by a sum over the bins

$$\hat{R}_{\rm E}^2(\Psi) = \frac{1}{2}\sum_{i=1}^{I}\frac{\Delta\vartheta_i}{\vartheta_i}\left[\hat{\xi}_+(\vartheta_i)\,Z_+(\vartheta_i,\eta) + \hat{\xi}_-(\vartheta_i)\,Z_-(\vartheta_i,\eta)\right], \quad (17)$$

with $\hat{\xi}_\pm(\vartheta_i)$ denoting the estimator of the ith 2PCF bin. The upper limit I in Eq. (17) denotes the bin up to which $\vartheta_i \le \Psi$. Inserting Eq. (17) into Eq. (16) we derive

$$\mathrm{C}_{\mathcal{R}}(\Psi_k,\Psi_l) = \sum_{i=1}^{I}\sum_{j=1}^{J}\frac{\Delta\vartheta_i\Delta\vartheta_j}{4\,\vartheta_i\vartheta_j} \times\left[\sum_{m,n=+,-}Z_m(\vartheta_i,\Psi_k)\,Z_n(\vartheta_j,\Psi_l)\,\mathrm{C}_{mn}(\vartheta_i,\vartheta_j)\right], \quad (18)$$

where I and J denote the bins up to which $\vartheta_i \le \Psi_k$ ($\vartheta_j \le \Psi_l$) holds.

Similarly a covariance for the general EB-statistics can be calculated as

$$\mathrm{C}_E(\Psi_k,\Psi_l) = \sum_{i=1}^{I}\sum_{j=1}^{J}\Delta\vartheta_i\Delta\vartheta_j\,\vartheta_i\vartheta_j \times\left[\sum_{m,n=+,-}T_m\left(\vartheta_i,\theta_k\right)\,T_n\left(\vartheta_j,\theta_l\right)\mathrm{C}_{mn}(\vartheta_i,\vartheta_j)\right]. \quad (19)$$

5.1. Correlation matrices

In order to illustrate the correlation between the individual data points we calculate the correlation matrix $\mathbf{R}$ for $\langle\mathcal{RR}_{\rm E}\rangle$, E, and $\langle M_{\rm ap}^2\rangle$ from the corresponding covariance matrix. For $\mathbf{C}$ being the covariance of either $\langle\mathcal{RR}_{\rm E}\rangle$, E, or $\langle M_{\rm ap}^2\rangle$ the correlation coefficients are defined as

$$\mathrm{R}_{ij} = \frac{\mathrm{C}_{ij}}{\sqrt{\mathrm{C}_{ii}\mathrm{C}_{jj}}}\,. \quad (20)$$

The covariances are calculated from a 2PCF ray-tracing covariance via Eqs. (15), (18), and (19), respectively. Finally the correlation matrix is obtained via Eq. (20). The ray-tracing simulations (175 realizations) have the following underlying cosmology: $\Omega_{\rm m} = 0.27, \Omega_\Lambda = 0.73, \sigma_8 = 0.78, h = 0.73, \Omega_{\rm b} = 0.044, n_{\rm s} = 1.0$. From now on we refer to this cosmological parameter set as our fiducial cosmological model $\boldsymbol{\pi}_{\rm fid}$. Survey parameters which enter in the calculation read as follows: galaxy density $n_{\rm gal} = 25/\mathrm{arcmin}^2$, survey area $A = 36\ \mathrm{deg}^2$, and intrinsic ellipticity noise $\sigma_\epsilon = 0.38$. The survey parameters differ slightly from those of the covariance used in the latest CFHTLS survey. FSH08 use $A = 34.2\ \mathrm{deg}^2$, $n_{\rm gal} = 13.3/\mathrm{arcmin}^2$, and $\sigma_\epsilon = 0.42$.

The covariance matrices have a different angular range corresponding to the data vectors of $\langle\mathcal{RR}_{\rm E}\rangle$, E, and $\langle M_{\rm ap}^2\rangle$, which we define as

$$\langle\boldsymbol{\mathcal{RR}}_{\mathbf{E}}\rangle = [\langle\mathcal{RR}_{\rm E}\rangle(\Psi_1),...,\langle\mathcal{RR}_{\rm E}\rangle(\Psi_n)]^{\rm t}\,, \quad (21)$$

$$\boldsymbol{E} = [E(\Psi_1),...,E(\Psi_n)]^{\rm t}\,, \quad (22)$$

$$\langle\boldsymbol{M}_{\mathbf{ap}}^{\mathbf{2}}\rangle = \left[\langle M_{\rm ap}^2\rangle(\theta_1),..,\langle M_{\rm ap}^2\rangle(\theta_m)\right]^{\rm t}. \quad (23)$$

Whereas $\langle\boldsymbol{\mathcal{RR}}_{\mathbf{E}}\rangle$ and $\boldsymbol{E}$ extend from $1' \le \Psi \le 460'$, $\langle\boldsymbol{M}_{\mathbf{ap}}^{\mathbf{2}}\rangle$ extends from $6' \le \theta \le 230'$. The different maximum angular separation of the aperture mass dispersion result from the fact that $\langle\mathcal{RR}_{\rm E}\rangle(\Psi)$ and $E(\Psi)$ contain information on the 2PCF with $\vartheta \le \Psi$, whereas $\langle M_{\rm ap}^2\rangle(\theta)$ contains information on the 2PCF up to $\vartheta \le 2\theta$. The lower limit of $6'$ was chosen to circumvent the problem of E/B-mode mixing for the $\langle M_{\rm ap}^2\rangle$ covariance. The range of the original 2PCF ray-tracing covariance extends from $0\farcm5 \le \vartheta \le 460'$. Below $6'$ it is not possible to calculate the $\langle M_{\rm ap}^2\rangle$ covariance properly.

Figure 3 shows the correlation matrices of the ring statistics (left), the EB-statistics (middle), and of the aperture mass dispersion (right). Starting from the diagonal, where $R_{ii} = 1$, the nth contour line corresponds to values of 0.8^n. It is clearly noticeable that data points of the ring statistics are significantly less correlated than those of the aperture mass dispersion and the EB-statistics.

The boxy contours in Fig. 3 result from the small number of bins we choose in the covariances. The reason for this is that the ray-tracing covariance is an estimated quantity, hence its inverse, needed for the likelihood analysis in Sect. 6, is in general affected from numerical artifacts. These artifacts become more severe in case of a high dimension matrix. In order to guarantee a stable inversion process we choose a small number of bins.

5.2. *S/N*

We now use the above derived covariances to quantify the S/N of the ring statistics, EB-statistics and compare both to that of the aperture mass dispersion.

We calculate a set of 2PCFs via Eq. (3) for an angular range similar to that of the ray-tracing simulations (see Sect. 5.1), i.e. $\vartheta \in [0\farcm5, 460']$. The required shear power spectra $P_{\rm E}$ are obtained from the density power spectra P_δ employing Limber's equation. As underlying cosmology we choose our fiducial model (see Sect. 5). The power spectrum P_δ is calculated from an initial Harrison-Zeldovich power spectrum ($P_\delta(k) \propto k^{n_{\rm s}}$) with the transfer function from Efstathiou et al. (1992). For the nonlinear evolution we use the fitting formula of Smith et al. (2003).

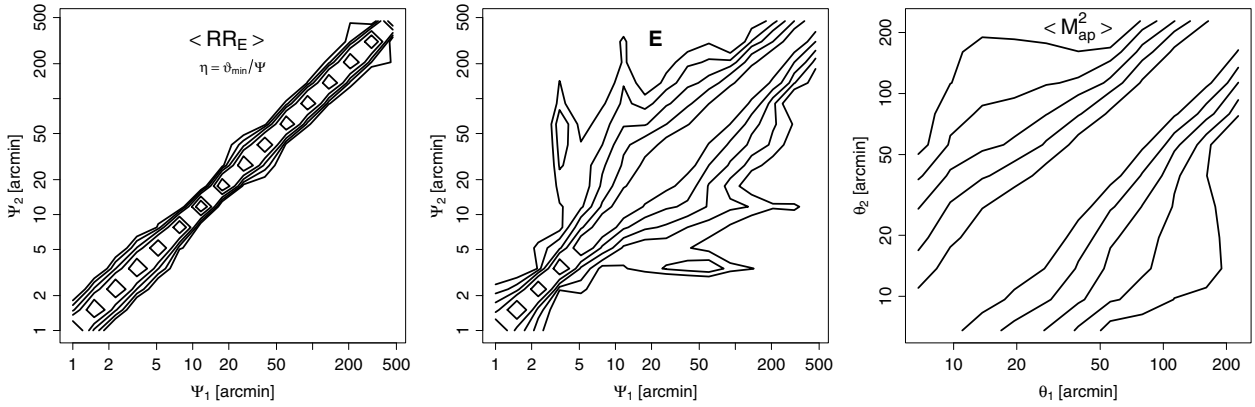

Fig. 3. This figure shows the correlation matrices of $\langle \mathcal{RR}_{\rm E} \rangle$ (*left*), E (*middle*), and $\langle M_{\rm ap}^2 \rangle$ (*right*) derived from ray-tracing 2PCF covariance matrix. In each panel the nth contour line (starting with $n = 1$ close to the diagonal) marks values of $(0.8)^n$.

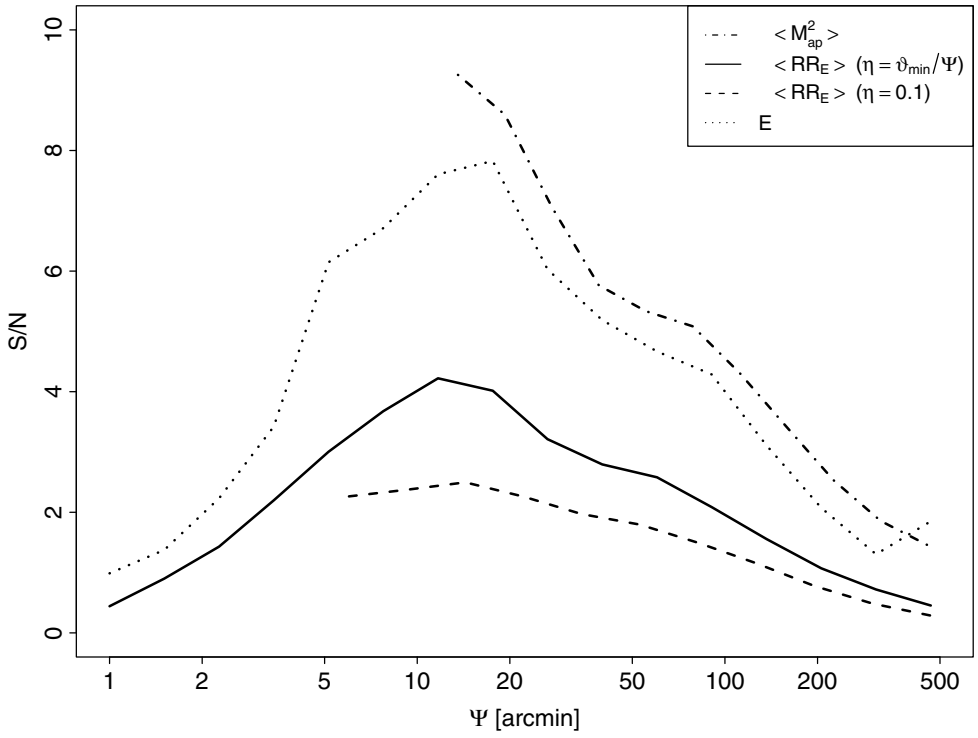

Fig. 4. The S/N of the ring statistics (for $\eta = 0.'5/\Psi$ and $\eta = 0.1$), the EB-statistics, and the aperture mass dispersion calculated from a set of theoretical 2PCFs with $\vartheta \in [0.'5; 460']$. The different angular range of the measures is explained in the text.

In the calculation of $P_{\rm E}$ we choose a redshift distribution of source galaxies similar to that of Benjamin et al. (2007)

$$n(z) = \frac{\beta}{z_0 \Gamma\left((1+\alpha)/\beta\right)} \left(\frac{z}{z_0}\right)^{\alpha} \exp\left[-\left(\frac{z}{z_0}\right)^{\beta}\right], \qquad (24)$$

with $\alpha = 0.836, \beta = 3.425, z_0 = 1.171$.

From this set of 2PCFs we calculate data vectors of $\langle \mathcal{RR}_{\rm E} \rangle$, E, and $\langle M_{\rm ap}^2 \rangle$ according to Eqs. (7) and (11), and (4), respectively. The angular range of these data vectors are chosen similar to the range of the corresponding covariances (Sect. 5.1), i.e. $0.'5 \leq \Psi \leq 460.'0$ for $\boldsymbol{\langle \mathcal{RR}_{\rm E} \rangle}$ and $\boldsymbol{E}$, and $6.'0 \leq \theta \leq 230.'0$ for $\boldsymbol{\langle M_{\rm ap}^2 \rangle}$. The S/N is calculated as

$$S/N = \frac{\langle \mathcal{RR}_{\rm E} \rangle(\Psi_i)}{[{\rm C}_{\mathcal{R}}(\Psi_i, \Psi_i)]^{1/2}} \quad \text{and} \quad S/N = \frac{\langle M_{\rm ap}^2 \rangle(\theta_i)}{[{\rm C}_{\mathcal{M}}(\theta_i, \theta_i)]^{1/2}} \,. \qquad (25)$$

The results are illustrated in Fig. 4. We compare the ring statistics for with scale-dependent η and $\eta = 0.1$ to the EB-statistics and the aperture mass dispersion. The figure shows the anticipated behavior (Sect. 3): The ring statistics with scale-dependent η gives a higher S/N compared to the case where η is fixed. In addition, it can be measured down to arbitrary small values of Ψ (above $\vartheta_{\rm min}$), which is not possible when choosing a fixed η. For the case considered here, i.e. $\vartheta_{\rm min} = 0.'5$, the choice of $\eta = 0.1$ already limits the range of Ψ to scales $\geq 5'$, and decreasing η further in order to increase the S/N will limit $\boldsymbol{\langle \mathcal{RR}_{\rm E} \rangle}$ to larger Ψ.

When comparing the ring statistics to the aperture mass dispersion, we find that the ring statistics' signal is lower. Even with the scale-dependent filter function the S/N of the ring statistics is on average by a factor of ≈ 2 lower than the S/N of the aperture mass dispersion. This difference can be explained when comparing the filter functions of $\langle \mathcal{RR}_{\rm E} \rangle$ and $\langle M_{\rm ap}^2 \rangle$, $Z_{\pm}$ (Fig. 2) and $T_{\pm}$ (e.g. Fig. 1 in Schneider et al. 2002b), respectively. The Z-functions have two roots at their boundaries whereas the T_+-function becomes particularly large for small x. However, we point out that the S/N does not solely determine the ability of

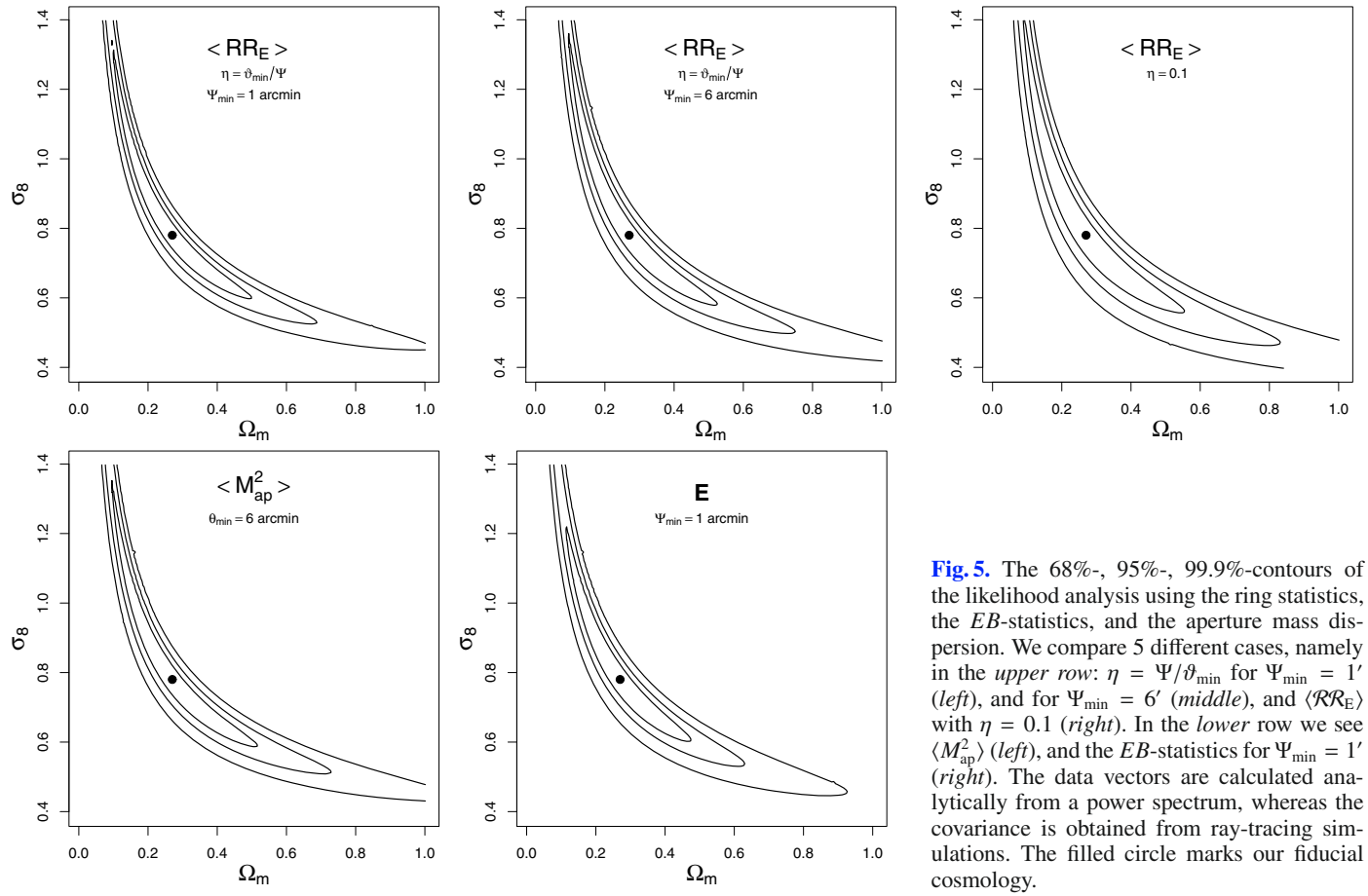

Fig. 5. The 68%-, 95%-, 99.9%-contours of the likelihood analysis using the ring statistics, the EB-statistics, and the aperture mass dispersion. We compare 5 different cases, namely in the *upper row*: $\eta = \Psi/\vartheta_{\rm min}$ for $\Psi_{\rm min} = 1'$ (*left*), and for $\Psi_{\rm min} = 6'$ (*middle*), and $\langle\mathcal{RR}_{\rm E}\rangle$ with $\eta = 0.1$ (*right*). In the *lower* row we see $\langle M_{\rm ap}^2\rangle$ (*left*), and the EB-statistics for $\Psi_{\rm min} = 1'$ (*right*). The data vectors are calculated analytically from a power spectrum, whereas the covariance is obtained from ray-tracing simulations. The filled circle marks our fiducial cosmology.

a measure to constrain cosmology, but one has to account for the fact that the data points of the $\langle\mathcal{RR}_{\rm E}\rangle$ are less correlated than those of $\langle M_{\rm ap}^2\rangle$. For a full comparison of the information content we examine both measures in a likelihood analysis.

Compared to the ring statistics the S/N of the EB-statistics is significantly higher on all scales, which again can be explained by the fact that the filter function of the EB-statistics does not have roots at their boundaries. Compared to the aperture mass dispersion, the EB-statistics' S/N is slightly lower. However, we point out that the EB-filter function, we chose here, is a simple second-order polynomial. We will present an extended analysis of this general EB-filter functions in a future paper.

6. Comparison of the information content of $\langle\mathcal{RR}_{\rm E}\rangle$ and $\langle M_{\rm ap}^2\rangle$

We now perform a likelihood analysis in the $\Omega_{\rm m}$ vs. σ_8 parameter space in order to compare the ability of $\langle\mathcal{RR}_{\rm E}\rangle$, E, and $\langle M_{\rm ap}^2\rangle$ to constrain cosmological parameters. We calculate 2PCF data vectors for various combinations of $\sigma_8 \in [0.4; 1.4]$ and $\Omega_{\rm m} \in [0.01; 1.0]$, therefrom derive the data vectors of $\langle\mathcal{RR}_{\rm E}\rangle$, E, and $\langle M_{\rm ap}^2\rangle$ and test these against the corresponding data vectors obtained from our fiducial model (Sect. 5.1). We assume that all data vectors are normally distributed in parameter space and calculate the posterior likelihood according to Bayes theorem. Our likelihood function $p(\boldsymbol{d}|\boldsymbol{\pi})$ then reads

$$p(\boldsymbol{d}|\boldsymbol{\pi}) = \frac{\exp\left[-\frac{1}{2}\left((\boldsymbol{d}(\boldsymbol{\pi}) - \boldsymbol{d}(\boldsymbol{\pi}_{\rm fid}))^{\rm t}\,\mathbf{C}^{-1}\,(\boldsymbol{d}(\boldsymbol{\pi}) - \boldsymbol{d}(\boldsymbol{\pi}_{\rm fid}))\right)\right]}{(2\pi)^{n/2}\,|\mathbf{C}|^{\frac{1}{2}}}, \quad (26)$$

where $\boldsymbol{d}$ must be replaced by the considered data vector, either $\langle\mathcal{RR}_{\rm E}\rangle$ (Eq. (21)), $\langle\boldsymbol{M_{\rm ap}^2}\rangle$ (Eq. (22)), or $\boldsymbol{E}$ (Eq. (23)).

To illustrate the information content we calculate the so-called credible regions, where the true parameter is located with a probability of 68%, 95%, 99,9%, respectively. In addition, we quantify the size of these credible regions through the determinant of the second-order moment of the posterior likelihood (see e.g. Eifler et al. 2008)

$$Q_{ij} \equiv \int {\rm d}^2\boldsymbol{\pi}\, p(\boldsymbol{\pi}|\boldsymbol{\xi})\,\left(\pi_i - \pi_i^{\rm f}\right)(\pi_j - \pi_j^{\rm f}), \quad (27)$$

where π_i are the varied parameters, $\pi_i^{\rm f}$ are the parameter of the fiducial model ($i = 1, 2$, corresponding to $\Omega_{\rm m}$ and σ_8). The square root of the determinant is given by

$$q = \sqrt{|Q_{ij}|} = \sqrt{Q_{11}Q_{22} - Q_{12}^2}, \quad (28)$$

and it can be considered as our figure of merit quantity. Smaller credible regions in parameter space correspond to a lower value of q. In this paper all q's are given in units of 10^{-4}. There are several differences between q and the more commonly used figure of merit introduced by the Dark Energy Task Force (DETF) (Albrecht et al. 2006). The DETF-FoM measures the reciprocal of the area of the error ellipse enclosing the 95% confidence limit in the plane of the dark energy parameters w_0 and w_a. Under the assumption of a Gaussian likelihood in parameter space the DETF-FoM can be calculated from the Fisher matrix. Fu & Kilbinger (2009) apply this concept to the $\Omega_{\rm m}$-σ_8 parameter plane, however, as can be seen in Fig. 5, the likelihood for this parameter combination is significantly skewed. Here, the Fisher

matrix approach can be a valid approximation very close to the fiducial model but is insensitive to the likelihood at the boundaries of the parameter space. Due to the Ω_m-σ_8 degeneracy the behavior of the likelihood within these outer parameter regions is important when quantifying the information content and we therefore perform a full likelihood analysis for each measure. From the obtained likelihood we then calculate q as described above.

Note that the value of q does not directly relate to or scale linearly with the enclosed area of the likelihood contours. Equation (27) shows that q is most sensitive to parameter regions which strongly deviate from the fiducial model. A large deviation in q can be caused by a comparably small deviation in the likelihood at the boundaries of the considered parameter space. This implies that q penalizes a measure if it cannot resolve a parameter degeneracy. This behavior is intended as breaking the Ω_m-σ_8 degeneracy is important for cosmic shear. In order to illustrate the significance of different q we show the likelihood contours of all measures in Fig. 5.

We employ the ray-tracing covariances in our likelihood analysis and choose the angular range of the data vectors correspondingly (Sect. 5.1), i.e. $\Psi \in [1'; 460']$ and $\theta \in [6'; 230']$. We further assume a flat prior probability with cutoffs, which means $p(\boldsymbol{\pi})$ is constant for all parameters inside a fixed interval ($\Omega_m \in [0.01; 1.0]$, $\sigma_8 \in [0.4; 1.4]$) and $p(\boldsymbol{\pi}) = 0$ else.

Our ray-tracing covariance automatically accounts for the non-Gaussianity of the shear field, however we neglect the cosmology dependence of the covariance (for more details see Eifler et al. 2009). Furthermore, we account for the bias which occurs during the inversion of the ray-tracing covariance by applying the correction factor outlined in Hartlap et al. (2007).

The upper row of Fig. 5 shows the result of the likelihood analysis for the ring statistics. We consider 3 cases: First, $\langle \mathcal{RR}_E \rangle$ with $\eta = \vartheta_{min}/\Psi$ and $\Psi \in [1'; 460']$ (left). Second, $\langle \mathcal{RR}_E \rangle$ with $\eta = \vartheta_{min}/\Psi$ and $\Psi \in [6'; 460']$ (middle). Third, $\langle \mathcal{RR}_E \rangle$ with $\eta = 0.1$ and $\Psi \in [1'; 460']$ (right). The lower row shows a similar analysis for $\langle M_{ap}^2 \rangle$ with an angular range $\theta \in [6'; 230']$ (left) and the EB-statistics for $\Psi \in [1'; 460']$ (right). The black, filled circle indicates the fiducial cosmology, and the contours correspond to the aforementioned credible regions. In addition we quantify the information content by the values of q, defined in Eq. (28), which are summarized in Table 1.

The ring statistics with $\eta = \vartheta_{min}/\Psi$ is a clear improvement over $\langle \mathcal{RR}_E \rangle$ with $\eta = 0.1$ which can be explained by the higher S/N of the first compared to the second. Considering the ring statistics with scale-dependent η, we find that adding information below $6'$ increases the information content of $\langle \mathcal{RR}_E \rangle$, such that it gives tighter constraints than the $\langle M_{ap}^2 \rangle$ data vector. The strength of this gain in information can be explained by the low correlation of ring statistics' data points.

In our analysis it was not possible to calculate $\langle M_{ap}^2 \rangle$ for $\theta \leq 6'$ due to the aforementioned E/B-mode mixing, however this can change if the 2PCF is measured on smaller angular scales. For this case we expect the improvement of ring statistics over the aperture mass dispersion to be even more significant. Due to the lower correlation of the ring statistics' data points an inclusion of smaller scales will enhance constraints from $\langle \mathcal{RR}_E \rangle$ stronger than those from $\langle M_{ap}^2 \rangle$.

The EB-statistics gives tighter constraints on cosmology than the optimized ring statistics, which can be explained by its higher S/N. However, we do not use the EB-statistics to analyze the CFHTLS data in the next section for the reason that the EB-statistics' data points are strongly correlated (see Fig. 3). In order to identify B-modes as a function of angular scale accurately, the lower correlation of the ring statistics is more useful.

Table 1. Values of q resulting from the likelihood analyses of the 5 data vectors.

Data vector	q
$\langle \mathcal{RR}_E \rangle$ ($\eta = \vartheta_{min}/\Psi$, $\Psi_{min} = 1'$)	153.8
$\langle \mathcal{RR}_E \rangle$ ($\eta = \vartheta_{min}/\Psi$, $\Psi_{min} = 6'$)	177.3
$\langle \mathcal{RR}_E \rangle$ ($\eta = 0.1$)	207.9
$\langle M_{ap}^2 \rangle$ ($\theta_{min} = 6'$)	169.8
E ($\Psi_{min} = 1'$)	122.5

7. Ring statistics with the CFHTLS

In Sect. 5.1 we have shown that the ring statistics' data points are significantly less correlated compared to data points of the aperture mass dispersion. Therefore, despite its lower S/N, the ring statistics provides an ideal tool to analyze B-mode contaminations depending on the angular scale. In this section we use the 2PCFs of the FSH08 analysis and therefrom calculate the ring statistics for a scale-dependent $\eta = \vartheta_{min}/\Psi$ and for $\eta = 0.1$. We performed a similar analysis for other cases of fixed η, which resulted in a significantly weaker signal.

The CFHTLS 2PCF was measured in 72 000 bins over an angular range of $0.'05 \leq \vartheta \leq 466'$. We calculate $\langle \mathcal{RR}_E \rangle$ (Eq. (7)) and $\langle \mathcal{RR}_B \rangle$ (Eq. (8)) in 60 logarithmic bins over a range $0.'5 \leq \Psi \leq 460.'0$. The error for the ith E/B-mode data point is calculated as $\sqrt{\mathbf{C}_{R_{E/B}}(\Psi_i, \Psi_i)}$, where $\mathbf{C}_{R_{E/B}}(\Psi_i, \Psi_i)$ is calculated from a Gaussian 2PCF covariance. This Gaussian covariance was calculated from a theoretical model using the same cosmology and survey parameters as in the FSH08 analysis. We do not employ the non-Gaussian correction of Semboloni et al. (2007) as this corrects the C_{++}-term in the 2PCF covariance, but not the C_{--}- and C_{+-}-terms. Here, we use the full 2PCF covariance in the analysis. Similar to FSH08 we do not consider systematic errors in our analysis which might lead to an underestimation of the error bars.

The results of our analysis are illustrated in Fig. 6. The three panels in the upper row show the ring statistics' E- and B-modes on (from left to right) small, intermediate and large scales of Ψ for the case of $\eta = \vartheta_{min}/\Psi$. The three panels in the lower row show the same analysis but for $\eta = 0.1$. The circled (red) data points correspond to the E-mode signal, the triangled (black) data points correspond to the B-mode signal.

We measure a robust E-mode shear signal, however we also find a significant B-mode contribution on small (around $2'$), intermediate ($16'$–$22'$), and large scales (right panel). On small scales E-and B-mode are of similar order. It should be stressed that such an analysis of small-scale contaminations is not feasible with the aperture mass dispersion, which, to avoid the E/B-mode mixing on small scales, involves a theoretical (therefore B-mode free) 2PCF in its calculation. This theoretical data extension, combined with the fact that the aperture mass dispersion data points are stronger correlated (Sect. 5) can hide possible small-scale contaminations in the data.

The B-mode contamination on large scales is also observed in the FSH08 analysis. In addition, we find a small B-mode on intermediate scales (between $16'$ and $22'$), otherwise these intermediate scales are mostly free of B-modes and give a robust E-mode signal. The low correlation of the individual data points leads to the oscillations in the amplitude of the shear signal. A

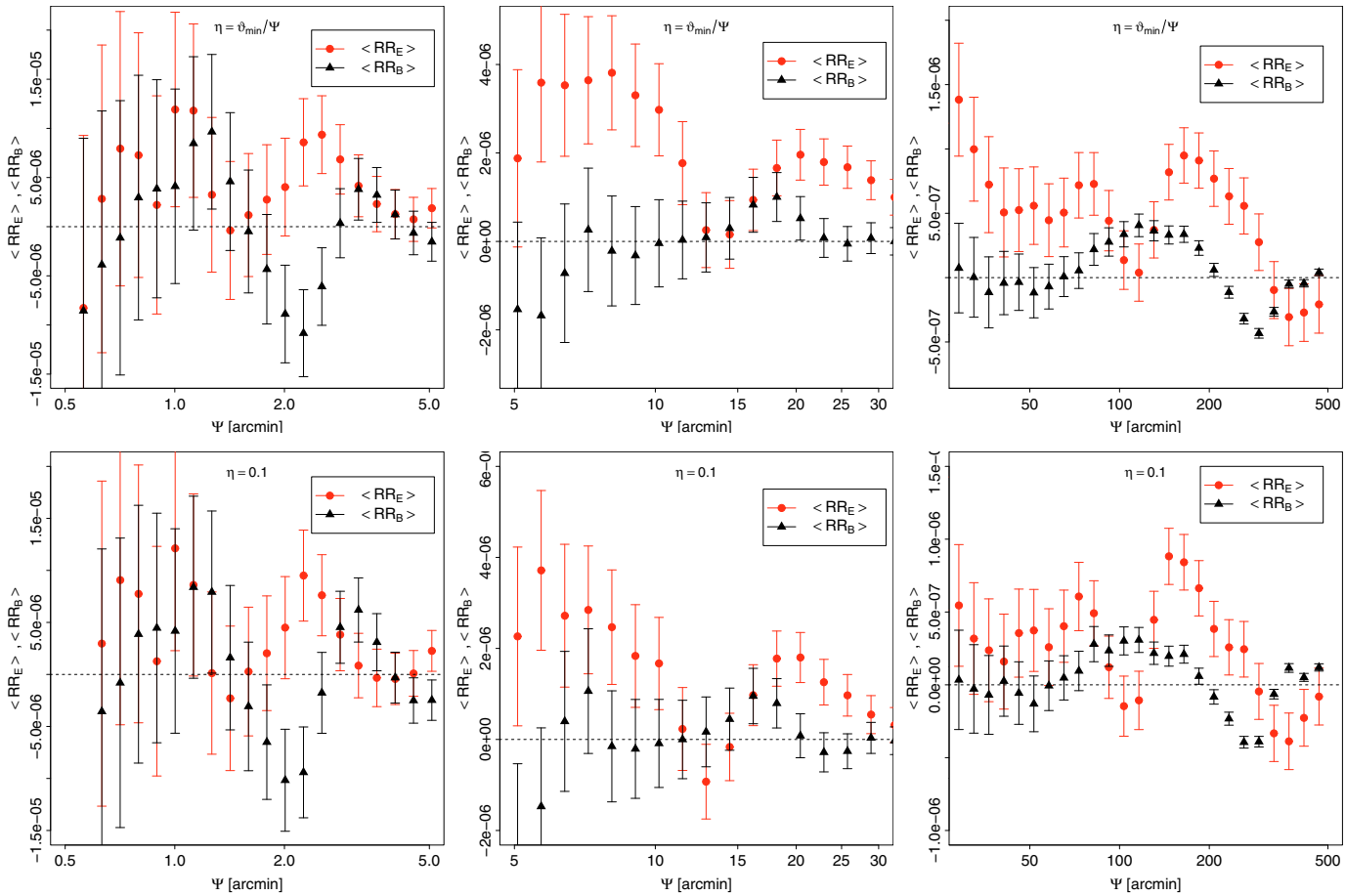

Fig. 6. The ring statistics signal measured from the CFHTLS for the case of $\eta = \vartheta_{\rm min}/\Psi$ (*upper row*). The red data points (circles) correspond to the E-mode signal, the black data points (triangles) to the B-mode signal. The three panels correspond to small (*left*), intermediate (*middle*), and large (*right*) scales. The *lower row* shows a similar analysis but for $\eta = 0.1$.

similar analysis with the aperture mass dispersion shows a much smoother behavior.

8. Conclusions

Decomposing the shear field into E- and B-modes is an important check for systematics in a cosmic shear analysis. The most commonly used methods for E- and B-mode decomposition, namely the aperture mass dispersion and the E/B-mode shear correlation function, require the 2PCF to be known down to arbitrary small or up to arbitrary large angular separations. In practice, the 2PCF is only measured over a finite interval $[\vartheta_{\rm min}; \vartheta_{\rm max}]$. As a result the aforementioned methods do not separate E- and B-modes properly, e.g. the aperture mass dispersion suffers from E/B-mode mixing on small angular scales (see KSE06 for further details).

In contrast, the ring statistics (invented in SK07) separates E- and B-modes properly using 2PCFs measured on a finite angular scale. As outlined in SK07 the filter functions of the ring statistics, i.e. $Z_{\pm}$, are in general complicated to calculate, and the authors restrict the free parameters this filter function to one, namely η. This parameter is held fixed, independent of the angular scale Ψ at which the ring statistics is evaluated. In this paper, we improve on the condition of a fixed η by choosing a scale-dependent $\eta = \vartheta_{\rm min}/\Psi$ which significantly improves on the ring statistics' S/N.

Furthermore, we present a formula to calculate the ring statistics' covariance from a 2PCF covariance. This formula is applied to a 2PCF covariance obtained from ray-tracing simulations. We therefrom calculate the correlation matrices of ring statistics and aperture mass dispersion and find that the data points of the first are significantly less correlated than the data points of the second. We employ these covariances to compare the information content of the two second-order statistics and find that the ring statistics' data points place tighter constraints on cosmological parameters than data points of the aperture mass dispersion. The reason for this is that we can include smaller scales in the ring statistics's data vector which is not possible for $\langle M_{\rm ap}^2 \rangle$ due to the aforementioned E/B-mode mixing. In addition, we consider a polynomial filter function which decomposes E- and B-modes on a finite interval and therefrom calculate an additional second-order measure, the EB-statistics. We compare the correlation of data points and the information content of this EB-statistics to the ring statistics and find that it shows a significantly higher correlation of the data points, but a higher information content. This can be explained by the high S/N of the EB-statistics.

We apply the ring statistics with $\eta = \vartheta_{\rm min}/\Psi$ and $\eta = 0.1$ to CFHTLS data, more precisely we calculate both from the 2PCF used in the latest CFHTLS analysis (FSH08). We measure a clear shear signal for $\eta = \vartheta_{\rm min}/\Psi$ which decreases when performing the same analysis for $\eta = 0.1$. The fact, that data points of the ring statistics have low correlations enables us to determine the contaminated scales very accurately. We find B-modes on large scales which is comparable to the findings of FSH08. In addition, we detect B-modes on intermediate (16′–22′) scales and a

scattered B-mode contribution on scales below 3′. In the latter case the shear signal is of the same order as the B-mode contribution.

A similar analysis with the aperture mass dispersion is only possible when including a 2PCF from a theoretical model in order to avoid the E/B-mode mixing on small angular scales. These added theoretical data can conceal remaining systematics (B-modes) which can be identified properly using the ring statistics. This property is most likely the most useful feature of the ring statistics. It can be used to detect remaining systematics very accurately in future surveys.

The noise-level of the ring statistics on small scales can be reduced by increasing the number of galaxy pairs within the contributing 2PCF-bins. The number of galaxy pairs inside a 2PCF-bin increases quadratically with $n_{\rm gal}$, therefore it would be interesting to test the ring statistics on a data set like e.g. the COSMOS survey. Similarly, an increased survey volume will significantly enhance the constraints, for the reason that the cosmic variance scales with $1/A$. For example, the CFHTLS data we consider here covers an area of 34.2 deg^2 with $n_{\rm gal} = 13.3$. Testing the ring statistics on the full CFHTLS sample (172 deg^2) would be an interesting project in the future.

Acknowledgements. The authors want to thank Yannick Mellier and Martin Kilbinger for useful discussions and advice. T.E. wants to thank Liping Fu for sharing her CFHTLS data and the Institut d' Astrophysique de Paris for its hospitality during the analysis of the CFHTLS data. This work was supported by the Deutsche Forschungsgemeinschaft under the projects SCHN 342/6–1 and SCHN 342/9–1. T.E. is supported by the International Max-Planck Research School of Astronomy and Astrophysics at the University Bonn.

Appendix A: $T_\pm$-functions

In order to define the $T_\pm$-functions used for the calculation of the EB-statistics we remap $\vartheta \in [\vartheta_{\rm min}; \vartheta_{\rm max}]$ to the $x \in [-1; 1]$ and define

$$x = \frac{2\,\vartheta - \vartheta_{\rm min} - \vartheta_{\rm max}}{\vartheta_{\rm max} - \vartheta_{\rm min}}\,, \tag{A.1}$$

$$B = \frac{\vartheta_{\rm max} - \vartheta_{\rm min}}{\vartheta_{\rm max} + \vartheta_{\rm min}}. \tag{A.2}$$

We choose our filter function $T_+(x)$ to be the lowest order polynomial which fulfills the two integral constraints of Eq. (13) and the normalization $\int_{-1}^{1} {\rm d}x\, T_+(x)\, T_+(x) = 2$. The function reads

$$T_+(x) = \frac{1}{\sqrt{Y}} \left(3\,B^2 - 5 - 6\,B\,x + 3\,(5 - B^2)\,x^2\right), \tag{A.3}$$

where

$$Y = \frac{8\,(25 + 5\,B^2 + 6\,B^4)}{5}\,. \tag{A.4}$$

Given the analytic form of T_+ the corresponding T_- is uniquely determined through Eq. (14).

References

Albrecht, A., Bernstein, G., Cahn, R., et al. 2006 [arXiv:astro-ph/0609591]
Bacon, D., Refregier, A., & Ellis, R. 2000, MNRAS, 318, 625
Bartelmann, M., & Schneider, P. 2001, Phys. Rep., 340, 291
Benjamin, J., Heymans, C., Semboloni, E., et al. 2007, MNRAS, 381, 702
Crittenden, R. G., Natarajan, P., Pen, U.-L., et al. 2001, ApJ, 559, 552
Crittenden, R. G., Natarajan, P., Pen, U.-L., et al. 2002, ApJ, 568, 20
Efstathiou, G., Bond, J. R., & White, S. D. M. 1992, MNRAS, 258, 1P
Eifler, T., Kilbinger, M., & Schneider, P. 2008, A&A, 482, 9
Eifler, T., Schneider, P., & Hartlap, J. 2009, A&A, 502, 721
Fu, L., & Kilbinger, M. 2009, MNRAS, in press [arXiv:0907.0795]
Fu, L., Semboloni, E., Hoekstra, H., et al. 2008, A&A, 479, 9
Hartlap, J., Simon, P., & Schneider, P. 2007, A&A, 464, 399
Heavens, A., Refregier, A., & Heymans, C. 2000, MNRAS, 319, 649
Hetterscheidt, M., Simon, P., Schirmer, M., et al. 2007, A&A, 468, 859
Heymans, C., Van Waerbeke, L., Bacon, D., et al. 2006, MNRAS, 368, 1323
Hilbert, S., Hartlap, J., White, S. D. M., et al. 2009, A&A, 499, 31
Hirata, C. M., & Seljak, U. 2004, Phys. Rev. D, 70, 063526
Hoekstra, H., Mellier, Y., van Waerbeke, L., et al. 2006, ApJ, 647, 116
Jain, B., Seljak, U., & White, S. 2000, ApJ, 530, 547
Jing, Y. P. 2002, MNRAS, 335, L89
Joachimi, B., & Schneider, P. 2008, A&A, 488, 829
Joachimi, B., & Schneider, P. 2009, A&A, 507, 105
Kaiser, N., Wilson, G., & Luppino, G. A. 2000, unpublished [arXiv:astro-ph/0003338]
Kilbinger, M., Schneider, P., & Eifler, T. 2006, A&A, 457, 15
King, L. J., & Schneider, P. 2003, A&A, 398, 23
Massey, R., Heymans, C., Bergé, J., et al. 2007a, MNRAS, 376, 13
Massey, R., Rhodes, J., Leauthaud, A., et al. 2007b, ApJS, 172, 239
Munshi, D., Valageas, P., van Waerbeke, L., et al. 2008, Phys. Rep., 462, 67
Schneider, P., & Kilbinger, M. 2007, A&A, 462, 841
Schneider, P., van Waerbeke, L., Kilbinger, M., et al. 2002a, A&A, 396, 1
Schneider, P., van Waerbeke, L., & Mellier, Y. 2002b, A&A, 389, 729
Schrabback, T., Erben, T., Simon, P., et al. 2007, A&A, 468, 823
Semboloni, E., Mellier, Y., van Waerbeke, L., et al. 2006, A&A, 452, 51
Semboloni, E., van Waerbeke, L., Heymans, C., et al. 2007, MNRAS, 375, L6
Smith, R. E., Peacock, J. A., Jenkins, A., et al. 2003, MNRAS, 341, 1311
van Waerbeke, L., & Mellier, Y. 2003 [arXiv:astro-ph/0305089]
van Waerbeke, L., Mellier, Y., Erben, T., et al. 2000, A&A, 358, 30
van Waerbeke, L., Mellier, Y., & Hoekstra, H. 2005, A&A, 429, 75
Wittman, D. M., Tyson, J. A., Kirkman, D., Dell'Antonio, I., & Bernstein, G. 2000, Nature, 405, 143